Acta Cryst. (1989). B**45**, 129–136

High-Resolution Electron Microscopy Study of the Superstructure of Xiuyan Jade and Matterhorn Surpentine

BY X. J. WU AND F. H. LI

Institute of Physics, Academia Sinica, Beijing, People's Republic of China

AND H. HASHIMOTO

Department of Mechanical Engineering, Okayama University of Science, Okayama 700, *Japan*

(*Received* 24 *May* 1988; *accepted* 2 *November* 1988)

Abstract

The crystal structures of antigorite contained in jade from Xiuyan, China, and surpentine from the Matterhorn, Switzerland, have been studied by electron diffraction and high-resolution electron microscopy together with elemental analysis. The superstructure model as well as the approximate coordinates of atoms have been set up on the basis of high-resolution electron microscopic images. The theoretical image contrast has been simulated and compared with the observed ones. The exact chemical formula and the influence of impurities on the structure are discussed.

1. Introduction

Antigorite [$Mg_6(Si_4O_{10})(OH)_8$] is a kind of layer silicate mineral built up from alternate layers of Si–O tetrahedra and brucite [$Mg(OH)_2$] (Fig. 1*a*) (Wang, Pan, Weng, Chen, Zhao, Chen, Ye, Dong, Xue, Yang & Lu, 1984; Cressey & Hutchison, 1983). Two-thirds of the hydroxyls at the base of each brucite layer are replaced by oxygens at the apices of SiO_4 tetrahedra. However, atoms of Mg, which occupy all the octahedral interstices surrounded by OH and O, are so large that the subcells have to bend along the *a* axis and form a wavy superstructure in order to compensate for the mismatch between the SiO_4 tetrahedra and brucite layers. The periodicity of the superlattice may range from tens to hundreds of ångstroms (Wang *et al.*, 1984). Antigorite was considered to possess a similar substructure to kaolinite [$Al_4(Si_4O_{10})(OH)_8$], whose structure is well known.

Kunze (1956, 1958) proposed three possible superstructure models for antigorite (Figs. 1*b*,*c*,*d*) based on X-ray diffraction analysis and gave a detailed discussion of the model shown in Fig. 1(*c*). He obtained the potential distribution projected along the *b* axis (Fig. 1*a*) by two-dimensional Fourier synthesis using structure amplitudes with indices *h*0*l* and pointed out that the radius of the curved subcell is about 75 Å and fourfold and eightfold links are formed in the superstructure. The space group was considered to be *Pm*. Yada (1979) published high-resolution electron microscopic images taken along the *b* axis, which confirmed the model shown in Fig. 1(*c*). Buseck & Cowley (1983) studied the modulated structure, and Cressey & Hutchison (1983) studied the domain structure and defects in antigorite by high-resolution electron microscopy (HREM).

Obviously, it is difficult to determine the crystal structure of antigorite completely by X-ray diffraction analysis because of the inevitable crystal defects and the weak reflections of the superstructure. However, the superstructure spots in the electron diffraction pattern (EDP) are usually strong enough to be observed, as the scattering power of electrons is stronger than that of X-rays. In addition, HREM enables direct observation of perfect regions of limited size in the crystal.

In the present paper electron diffraction and HREM investigations of the crystal structure of antigorite collected from the Xiuyan district of China and from the Matterhorn mountain in Switzerland are reported.

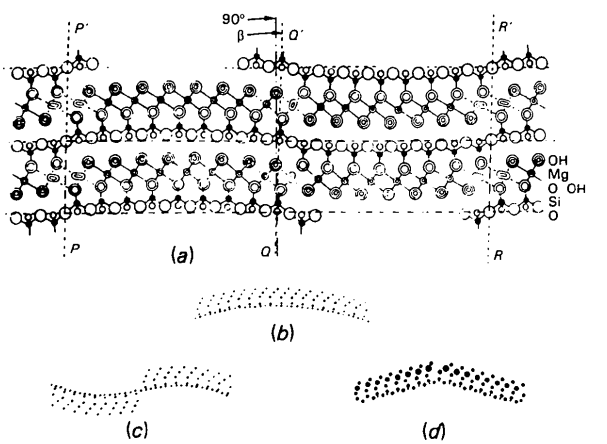

Fig. 1. (*a*) Atom positions projected along the *b* axis in antigorite. (*b*), (*c*), (*d*) Three structure models proposed for antigorite (Kunze, 1956, 1958).

0108-7681/89/020129-08$03.00

2. Experimental

Two kinds of antigorite samples have been studied. One is Xiuyan jade, which was collected in Xiuyan, China, the other is surpentine from the Matterhorn, Switzerland. Two kinds of TEM specimens, fine-fractured particles and thin cross sections of cleaved planes, were prepared.

The fine-fractured particles were made by grinding the crystal in agate mortar, dispersion in alcohol and then placing a drop of the resultant suspension on a microgrid. A small amount of gold was evaporated onto microgrids for obtaining the electron diffraction camera constant. Since the crystals always cleave along the (001) plane, only the projection along the c axis could be observed. In order to observe the cross section of the cleaved planes, the crystals were embedded in plastic, cut into slices and the slices polished down to 30–40 μm in thickness. The final thinning was performed by ion milling.

A JEM-200CX high-resolution electron microscope equipped with a top-entry goniometer was used for the observations. The accelerating voltage of the illuminating electrons was 200 kV and the spherical aberration of the objective lens was 1·2 mm.

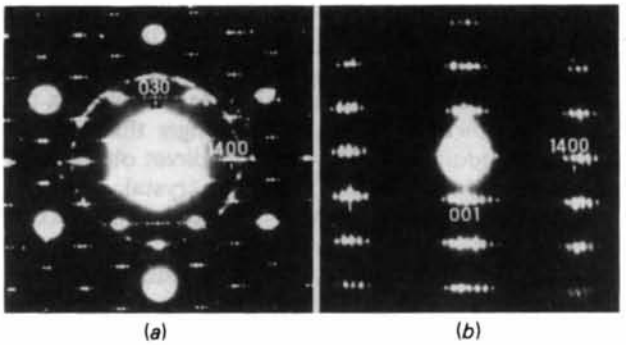

(*a*) (*b*)

Fig. 2. Electron diffraction patterns of antigorite in Xiuyan jade. (*a*) Projected along the c axis and (*b*) projected along the b axis.

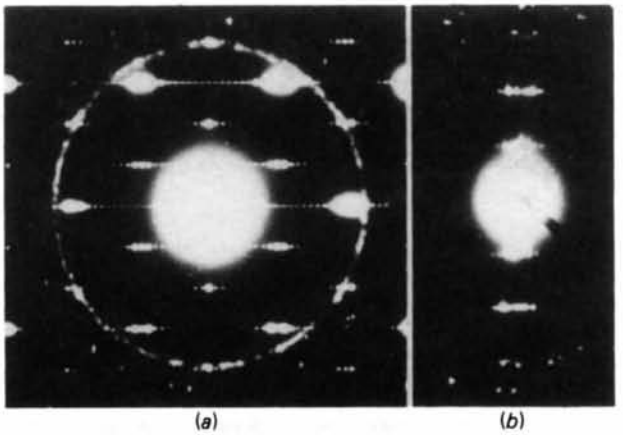

(*a*) (*b*)

Fig. 3. Electron diffraction patterns of Matterhorn surpentine. (*a*) Projected along the c axis and (*b*) projected along the b axis.

Table 1. *Unit-cell parameters*

	a (Å)	b (Å)	c (Å)	β (°)
Antigorite	33·7, 38·3 43·5, 109	9·26	7·28	91·6
Xiuyan jade	38·5	9·24	7·25	92·5
Matterhorn surpentine	53·5	9·27	7·16	93·

Table 2. *Composition and density of the samples*

	Component (wt%)						Density
	Si	Mg	Al	Fe	Ca	Mg/Si	(g cm^{-3})
Antigorite	20·3	26·3	0	0	0	1·30	2·60–2·70
Xiuyan jade	20·6	25·7	0·03	0·24	0·13	1·25	2·66
Matterhorn surpentine	18·3	21·8	0·72	5·20	2·30	1·19	2·64

3. Unit-cell parameters and chemical composition of Xiuyan jade and Matterhorn surpentine

The external forms of Xiuyan jade and Matterhorn surpentine are very different. Xiuyan jade is a beautiful stone with light-green colour and homogeneous fine texture. There is no clear defects on its surface. Matterhorn surpentine is inhomogeneous and dark green in colour with small black or white regions. However, their crystal structures possess some common features as shown in the following.

Figs. 2 and 3 show EDP's of the main phase in Xiuyan jade and Matterhorn surpentine, respectively. The diffraction rings in Figs. 2(*a*) and 3(*a*) are due to small crystals of Au deposited on the specimen-supporting grid. The unit-cell parameters determined from the EDP's are listed in Table 1. There were no forbidden reflections. This indicated that the possible space groups were Pm, $P2$ or $P2/m$. Both minerals belong to the monoclinic system and their b and c axes and β angles are similar and also close to those of antigorite (Wang *et al.*, 1984). According to the data given by Wang *et al.* (1984), the length of the a axis of antigorite is different from sample to sample, but the various a-axis lengths have a common divisor of about 5–5·7 Å (Table 1), equal to the subcell dimension along the a axis. This shows that the superlattice of antigorite consists of various stackings. The a axis of Xiuyan jade is about seven times and that of Matterhorn surpentine about ten times as large as the above-mentioned common divisor. Hence, these two minerals can be considered as different stackings of antigorite. Further evidence for the agreement of Xiuyan jade and Matterhorn surpentine with antigorite is obtained from the chemical analyses shown in Table 2. The small differences in composition from that of antigorite are due to minor phases or impurities.

4. High-resolution electron microscope images and structure models

Fig. 4 is a high-resolution image taken along the b axis of the antigorite in Xiuyan jade. The planar defects along the (001) plane indicated by arrows show the

weak connection between the neighbouring domains on either side of the (001) planes, so that the crystal is easily cleaved along the (001) plane.

Since the crystal is seriously damaged by electron-beam irradiation, becoming amorphous after a few seconds, it was not easy to take a series of through-focus images and the images obtained were often noisy. Two images taken along the *c* axis with different defocus are shown in Fig. 5, the focus step being about 400 Å. The noise of the micrographs was eliminated by translational superposition. The variation of the image contrast along the *a* axis bound to the superstructure (marked in Fig. 5*b*) has the following characteristics: (1) there are seven white dots in one period; (2) these white dots are not arranged equidistantly and they do not have the same intensity, for instance, the white dot located at the centre of the rectangle is stronger than the others; (3) there is a mirror symmetry parallel to (010) plane and no twofold axis along the *b* axis. In addition, the focus variation does not have a drastic effect on the image contrast.

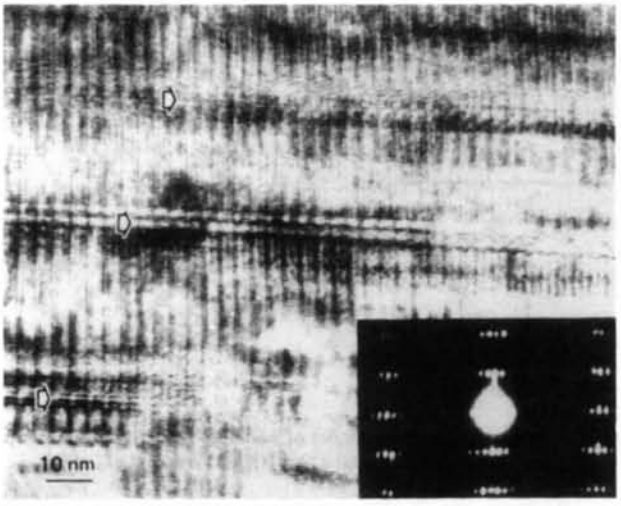

Fig. 4. High-resolution image and diffraction pattern of antigorite in Xiuyan jade projected along the *b* axis.

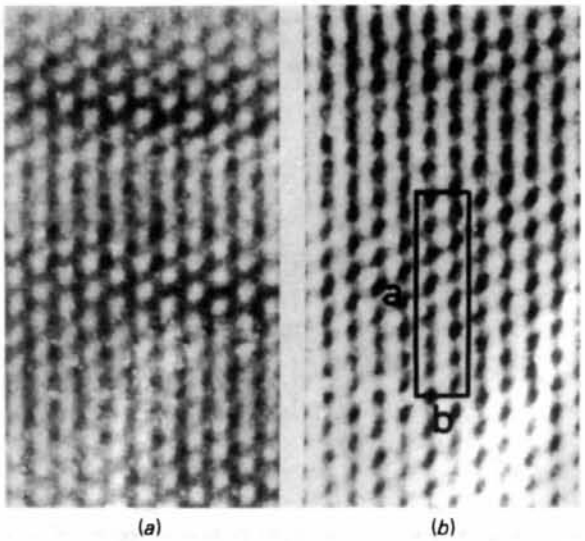

(*a*) (*b*)

Fig. 5. High-resolution images of antigorite in Xiuyan jade projected along the *c* axis. The focus difference between (*a*) and (*b*) is about 400 Å.

Fig. 6 is an HREM image of the antigorite of Matterhorn surpentine projected along its *c* axis. It has similar features to the images taken with the Xiuyan jade. The only difference is that along the *a* axis there are ten white dots per period instead of seven. This confirms that the two minerals have the same basic structure but different periods of superlattice.

The space group of both minerals can be determined as *Pm* owing to the absence of a twofold axis along the *b* axis in the images. This is in agreement with the results obtained by Kunze (1958).

Among the constituent atoms of antigorite, Si atoms are the heaviest. Hence, the crystal may be approximately treated as a weak-phase object (Spence, 1980) up to thicknesses of about 100 Å. As shown below it can be demonstrated that the hexagonal regions surrounded by SiO_4 tetrahedra, where all atoms are lighter than Si, appear as white dots in high-resolution images taken near the optimum defocus when the incident beam is parallel to the *c* axis. Hence, the superlattice of antigorite in Xiuyan jade consists of seven subcells per period while that in Matterhorn surpentine consists of ten subcells per period.

Both kaolinite and antigorite are layer-silicate minerals. The lattice parameters of kaolinite are close to the parameters of the subcell in antigorite. Hence, it seems reasonable to assume that the positions of the

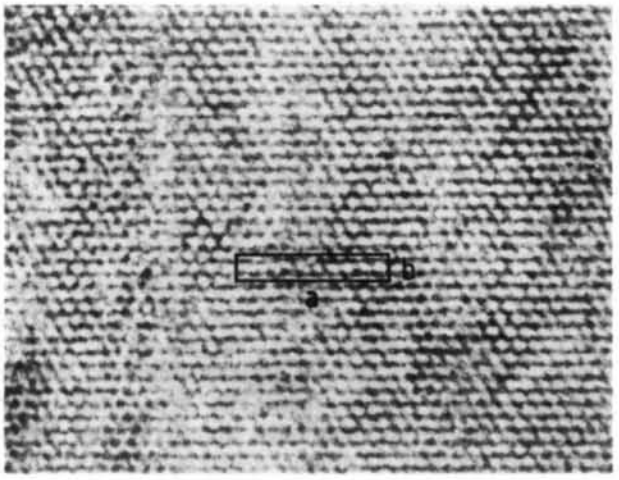

Fig. 6. High-resolution image of antigorite of Matterhorn surpentine projected along the *c* axis.

atoms in the subcell of antigorite are similar to those of kaolinite (see Fig. 7). The differences between the structures are in the number of octahedral interstices which are occupied by atoms of Al in kaolinite but by much larger atoms of Mg in antigorite. This leads to a slight mismatch of dimensions between layers of SiO_4 tetrahedra and layers of brucite. In order to compensate for the mismatch, bending of both layers occurs along the a axis. The alternate alignment of double layers, which become curved along the c axis positively (R_1) and negatively (R_2), forms a wavy superstructure along the a axis (Fig. 8). The construction of turning regions of curved double layers is essential for the superstructure model. Two possible types of turning regions are shown in Fig. 9 where the small horizontal arrows denote the atomic displacement caused by the bending of double layers. The symmetry at the turning plane for the two types is different. There is a twofold symmetry axis in Fig. 9(a), but only a twofold screw axis in Fig. 9(b). If the white dots in the images taken near the Scherzer focus are considered as hexagonal regions surrounded by SiO_4 tetrahedra, a white dot would be stronger than usual at the turning region shown in Fig. 9(a), while for that shown in Fig. 9(b) a weak white dot would appear. In the high-resolution images shown in Figs. 5 and 6, and especially in Fig. 11, both large and small white dots are seen. Therefore it is reasonable to assume that both of the types of turning region shown in Fig. 9 occur in antigorite.

There should be 36 atoms in one subcell of antigorite, namely, four Si atoms, ten O atoms, six Mg atoms and eight hydroxyls. The alternate alignment of double layers leads to some variation in the numbers of atoms at the turning regions. This introduces three additional atoms for each unit cell. The total number of atoms in each unit cell is

$$N(\text{total}) = 36m+3,$$

where m is the number of subcells per period. The numbers of the different kinds of atoms and of hydroxyls can be counted from Fig. 10 and are given by

$$N(\text{Si}) = 4m+2; \quad N(\text{O}) = 10m+5;$$
$$N(\text{Mg}) = 6m; \quad N(\text{OH}) = 8m-2.$$

It is obvious that the crystal is neutral if the chemical valence and numbers of atoms and hydroxyls per unit cell are summed. In the antigorite from Xiuyan jade, $m = 7$, so that $N(\text{total}) = 255$, $N(\text{Si}) = 30$, $N(\text{O}) = 75$, $N(\text{Mg}) = 42$, $N(\text{OH}) = 54$. In the antigorite from Matterhorn surpentine, $m = 10$, $N(\text{total}) = 363$, $N(\text{Si}) = 42$, $N(\text{O}) = 105$, $N(\text{Mg}) = 60$, $N(\text{OH}) = 78$.

Fig. 10 shows the atomic positions obtained for the antigorite from Xiuyan jade. The upper and lower diagrams are projections onto the (010) and (001) planes, respectively. O atoms located between two SiO_4 tetrahedra were not drawn in the (001) plane projection. This model satisfies Pm symmetry.

5. Simulated images and structure determination

It is necessary to record the coordinates of all atoms inside the unit cell to calculate images. This is much simplified by assuming that the brucite and tetrahedral double layers in antigorite are bent in accordance with a cylindrical shell of radius $R = 75$ Å (as shown in Fig. 8) and that the axis of the cylinder is parallel to the b axis.

O atoms which have the coordinate $Z_O = 0$ in the subcell will distribute uniformly on the surface of the cylinder of radius 75 Å, but all Si atoms will distribute

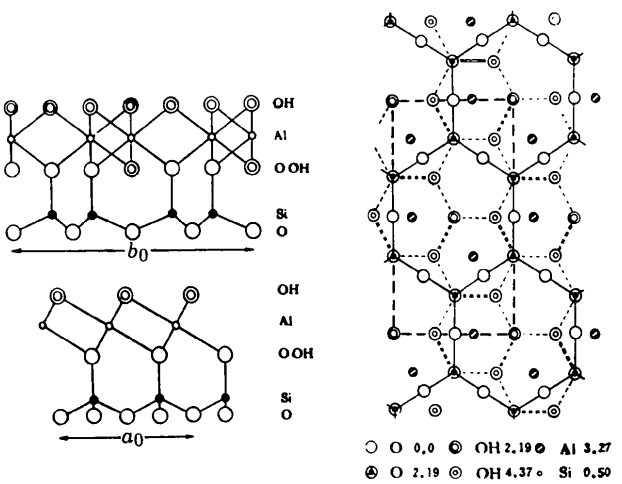

Fig. 7. Projected structure model of kaolinite along the a axis (top left), b axis (bottom left) and c axis (right) (Wang *et al.*, 1984).

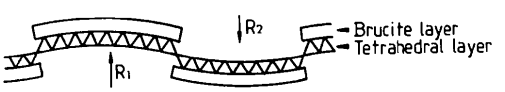

Fig. 8. Schematic diagram showing alternate alignment of curved brucite and tetrahedral double layers along the a axis in antigorite. R_1 and R_2 represent positive and negative curvatures respectively.

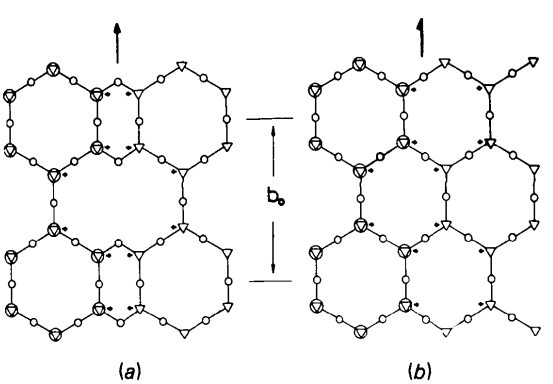

Fig. 9. (a), (b) Two possible types of turning regions of curved layers along the c axis. Small horizontal arrows denote slight displacements of atoms caused by the bending of brucite and tetrahedral double layers in antigorite.

uniformly on the surface of a cylinder of radius $(75 + Z_{Si})$ Å, where Z_{Si} denotes the coordinate of atoms Si along the c axis of the subcell. The arrangement of all other atoms obeys a similar rule.

Figs. 11 and 12 are HREM images taken along the c and b axes, respectively, for the antigorite from Xiuyan jade together with the corresponding simulated images obtained by the multislice method (Goodman & Moodie, 1974). The crystal thicknesses of the simulated images are 87 and 120 Å for Figs. 11 and 12, respectively. Comparison of the images in Fig. 11 with the projected structure model shown in Fig. 10, shows that the positions of the white dots in high-resolution images represent the hexagonal regions surrounded by SiO_4 tetrahedra. The larger dots represent octagonal regions, while all others are hexagonal regions. The quadrilateral regions cannot be seen under the present imaging conditions in both observed and simulated images. This is because the surrounding SiO tetrahedra which form the quadrilateral regions are too close. Fig. 13 is an image taken along the c axis for the antigorite from Matterhorn surpentine; the simulated image, which corresponds to a crystal thickness of 86 Å, is shown as an inset. A similar structural feature to that in Fig. 11 can be observed except for the longer periodicity along the a axis. These image contrast calculations suggest that the above-constructed structure models for antigorite are correct although the accuracy of the atomic coordinates is limited by the electron microscope images.

6. Image contrast change with crystal thickness

It is found from the simulated images that the image contrast of the present crystals is not so sensitive to the

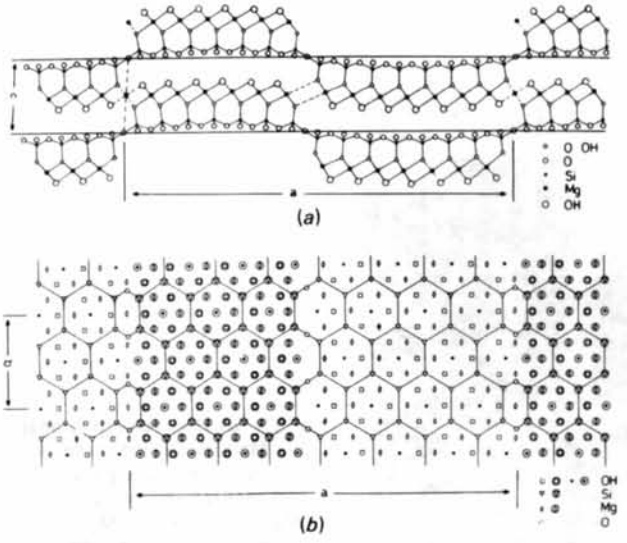

Fig. 10. Two projections of the atomic positions of Xiuyan jade onto the (*a*) (010) and (*b*) (001) planes.

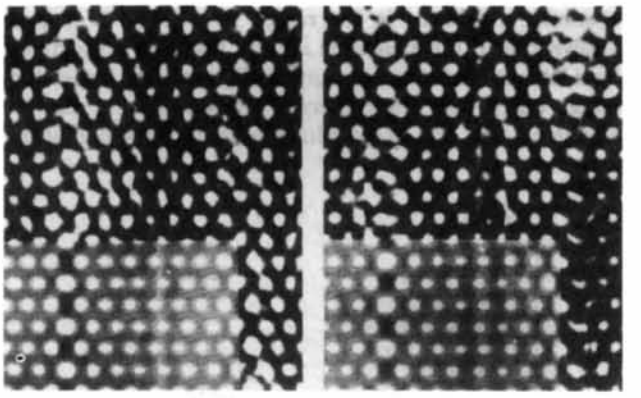

(*a*) (*b*)

Fig. 11. High-resolution images of Xiuyan jade projected along the c axis together with the calculated images for thickness 87 Å, underfocus (*a*) 900 Å and (*b*) 950 Å.

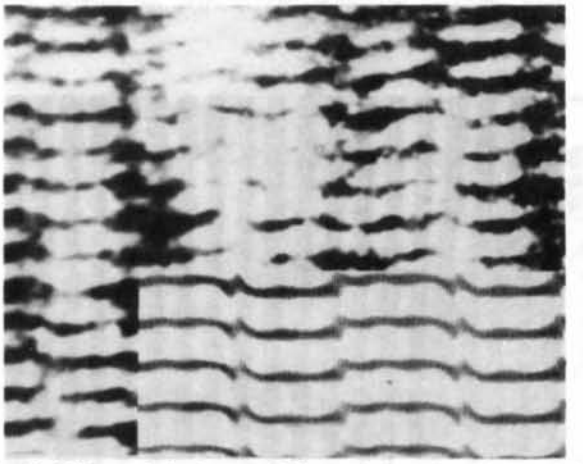

Fig. 12. High-resolution image of Xiuyan jade projected along the b axis with the calculated image for underfocus 100 Å and thickness 120 Å.

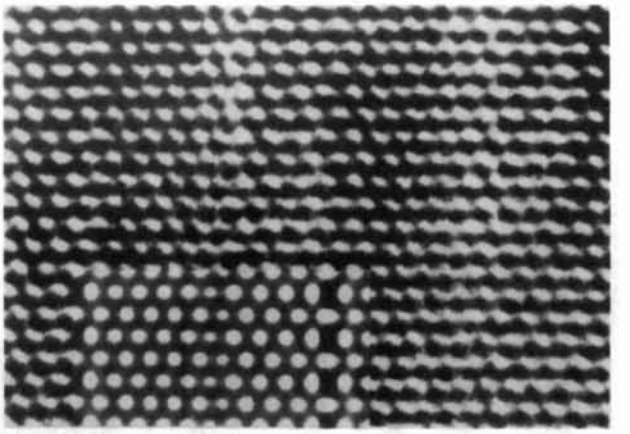

Fig. 13. High-resolution image of Matterhorn surpentine projected along the c axis together with the calculated image for underfocus 900 Å and thickness 86 Å.

specimen thickness in the range 10–100 Å. It is well known that if the specimen is very thin and consists of light atoms and also the unit cell is rather large, the image taken near the Scherzer focus condition can be explained by the weak-phase object approximation (WPOA). In this case the image contrast is approximately proportional to the projected potential distribution, namely the heavier atoms appear with darker contrast in the image. However, if the specimen thickness is larger than the critical value the contrast of heavy atoms reverses and the image may not resemble the projected potential (Li & Tang, 1985), so that the WPOA does not hold anymore. Fig. 14 shows the thickness dependence of amplitudes of strong diffracted beams from Xiuyan jade crystal calculated by the multislice method. Amplitudes of four strong waves

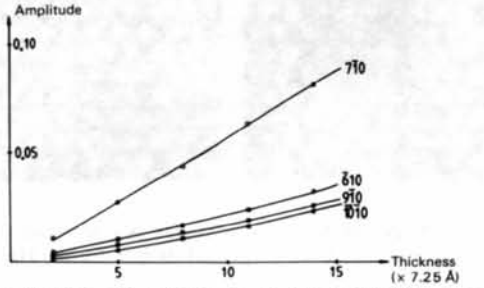

Fig. 14. Thickness dependence of amplitude of diffracted waves from (7$\bar{1}$0), ($\bar{6}$10), (9$\bar{1}$0) and ($\bar{1}$0$\bar{1}$0) of Xiuyan jade calculated by using multislice dynamical theory. Note the linearity up to thicknesses larger than 100 Å.

Table 3. *Comparison of experimental and calculated compositions and densities*

	Component (wt%)						Density
	Si	Mg	Al	Fe	Ca	Mg/Si	(g cm^{-3})
Xiuyan jade	20·6	25·7	0·03	0·24	0·13	1·25	2·66
Model of $Mg_{42}Si_{30}O_{75}(OH)_{54}$	21·2	25·6	0	0	0	1·21	2·59
Matterhorn surpentine	18·3	21·8	0·72	5·20	2·30	1·19	2·64
Model of $Mg_{860}Si_{42}O_{105}(OH)_{78}$	20·9	25·8	0	0	0	1·24	2·64

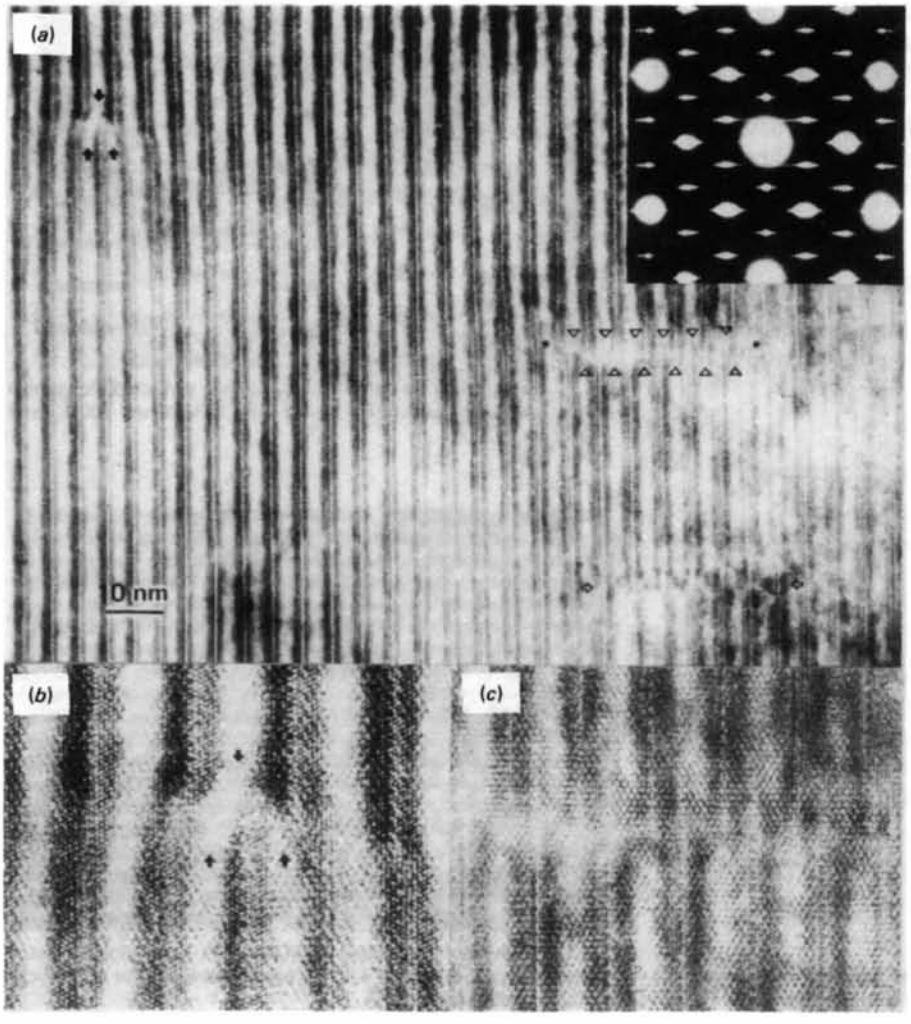

Fig. 15. (*a*) High-resolution image of Matterhorn antigorite with electron diffraction pattern (inset) showing the defects such as edge dislocations and extended dislocations with stacking faults. (*b*), (*c*) Enlargements of the defect regions.

increase almost linearly with increasing thickness and do not reach their maximum value even when the thickness is more than 100 Å. This means that the critical thickness for Xiuyan jade under the present imaging conditions is rather large, so that the correct image contrast, which is approximately proportional to the scattering power of the constituent atoms, can be obtained in a wide range of specimen thicknesses. This makes the crystal structure determination by HREM much easier.

7. Molecular formula and influence of impurities

Generally, the molecular formula of antigorite is written as $Mg_6Si_4O_{10}(OH)_8$. However, the superstructure model proposed above shows that there are slight differences in the ratio of elements for antigorites with different stackings. The molecular formula of antiogrite is a function of the number of subcells per unit cell (m) and the exact molecular formula is $Mg_{6m}Si_{4m+2}O_{10m+5}(OH)_{8m-5}$. For instance, it should be $Mg_{42}Si_{30}O_{75}(OH)_{54}$ and $Mg_{60}Si_{42}O_{105}(OH)_{78}$ for antigorite from Xiuyan jade ($m = 7$) and Matterhorn surpentine ($m = 10$) respectively. It is obvious that the general molecular formula, written as $Mg_6Si_4O_{10}(OH)_8$, corresponds to an infinite period of the superlattice, *i.e.* $m = \infty$.

A comparison of the measured composition and density with the values calculated in accordance with the standard chemical formulae is given in Table 3. The experimental results are in rather good agreement with the calculated ones. The difference in wt% of Si and Mg between calculated and experimental results for Matterhorn antigorite may be due to impurities.

The difference in the kind and number of impurity atoms may lead to the different period of the superlattice. It is known that the ionic radii of Mg^{2+}, Al^{3+}, Fe^{2+} and Ca^{2+} are 0·86, 0·67, 0·75 and 1·14 Å, respectively (Shannon & Prewitt, 1969). Among the three kinds of major impurities (Al, Fe and Ca), the Ca^{2+} ion is too large to replace the Mg^{2+} ion in the octahedral interstices, so that Ca may form another minor phase together with other elements. Fe^{2+} and Al^{3+} ions are smaller than the Mg^{2+} ion and can occupy the octahedral interstices. If Mg^{2+} ions are replaced by Fe^{2+} or Al^{3+}, the antigorite crystal should be less bent, and flatter than the structures proposed before (Wang *et al.*, 1984). In the latter case, two Al^{3+} ions would replace three Mg^{2+} ions. Hence, the radius of each bent layer would not be exactly constant, for instance, 75 Å as assumed above. The increase of Al and Fe will make the radius increase. As a result of the bending of the brucite and tetrahedral layers, the coordinates of corresponding atoms in different subcells would be different along the c direction. In order for the translational period to be constant, the coordinates of corresponding atoms in different subcells along the c direction should have a maximum value which is limited by the c parameter of antigorite. If this maximum value is assumed to be a constant for antigorite, it can be seen that the different radius will cause a different superperiod, *i.e.* the larger the radius, the longer the period of superstructure. This means that in the antigorite crystal the larger the number of Al or Fe atoms, the longer the superperiod. This could explain why the superperiod in Matterhorn antigorite is longer than that in Xiuyan jade.

It was observed in the low-magnification images that the two antigorites do not have obvious differences. However, in the high-magnification image shown in Fig. 15, it is seen that there are many defects in Matterhorn antigorite. In these areas the period of the superstructure along the a axis is changed. The elongation of the diffraction spots along the a axis observed in the inset EDP seems to be due to these defect structures and indicates that the period of the superstructure is not constant but variable in a certain range. The varied superperiod in antigorite from Matterhorn surpentine can be explained as the result of an inhomogeneous distribution of impurity elements. It can be concluded from the above observations that the regions with longer superstructure periods contain more Al and Fe impurity atoms.

8. Summary

The high-resolution electron microscope and electron diffraction study indicates that Xiuyan jade and Matterhorn surpentine belong to the antigorite family and have the chemical compositions $Mg_{42}Si_{30}O_{75}(OH)_{54}$ and $Mg_{60}Si_{42}O_{105}(OH)_{78}$, respectively. The difference in their chemical compositions is due to the difference in the period of the superstructure. The general formula for the chemical composition of a mineral of this family is $Mg_{6m}Si_{4m+2}O_{10m+5}(OH)_{8m+2}$, where m is the number of subcells in one period of the superstructure. The structural differences have been attributed to the number and kind of impurity atoms such as Al and Fe.

The authors are grateful to Drs G. N. Chang, X. H. Wang and S. T. Tang for carrying out the chemical analyses. XJW and FHL acknowledge helpful discussions with Professor J. L. Zhou. The project is supported by the National Natural Science Foundation of China.

References

BUSECK, R. & COWLEY, M. (1983). *Am. Mineral.* **68**, 18–40.
CRESSEY, B. A. & HUTCHISON, J. L. (1983). Inst. Phys. Conf. Ser. No. 68, ch. 10, pp. 409–412. Bristol: Institute of Physics.
GOODMAN, P. & MOODIE, F. (1974). *Acta Cryst.* A**30**, 280–293.
KUNZE, G. (1956). *Z. Kristallogr.* **108**, 82–107.
KUNZE, G. (1958). *Z. Kristallogr.* **110**, 282–320.

LI, F. H. & TANG, D. (1985). *Acta Cryst.* A41, 376–382.
SHANNON, R. D. & PREWITT, C. T. (1969). *Acta Cryst.* B25, 923–946.
SPENCE, J. (1980). *Experimental High Resolution Electron Microscopy*, pp. 85–88. Oxford Univ. Press.
WANG, P., PAN, Z. L., WENG, L. B., CHEN, D. C., ZHAO, A. X., CHEN, S. X., YE, Z. H., DONG, Z., XUE, J. Z., YANG, Z. Y. & LU, R. Y. (1984). *Systematic Mineralogy* (in Chinese), Vol. 2, pp. 380–394. Beijing: Geology Publishing House.
YADA, K. (1979). *Can. Mineral.* 17, 679–691.

Acta Cryst. (1989). B45, 136–141

A Transmission Electron Microscope Study of Modulated Sodium Lithium Metasilicates

BY R. L. WITHERS, J. G. THOMPSON AND B. G. HYDE

Research School of Chemistry, Australian National University, GPO Box 4, Canberra, ACT 2601, Australia

(*Received* 20 *July* 1988; *accepted* 24 *November* 1988)

Abstract

High-$Na_{2-x}Li_xSiO_3$, $0{\cdot}86 \le x \le 1{\cdot}02$, occurs as a modulated structure, the subcell of which is equivalent to the unit cells of Na_2SiO_3 and Li_2SiO_3 (orthorhombic, $Cmc2_1$), with the primary modulation wavevector directed along **b***. A satellite extinction condition observed at the [100] zone axis implies that the primary component of the incommensurate modulation involves an antiphase relationship between the modulations associated with sites related by a mirror plane perpendicular to the **a** axis. This antiphase relationship provides an explanation for the limited composition range of existence of this modulated phase. The modulation periodicity, while composition dependent, clearly can *not* be directly related to the Na : Li ratio. Less-rapidly cooled specimens show planar boundaries perpendicular to **b** and are interpreted as incipient high→low transition, resulting in breaking the above condition and streaking along **b***.

Introduction

An X-ray diffraction study of phase equilibria in the system $Na_2SiO_3 + Li_2SiO_3$ by West (1976, 1977) revealed a modulated structure for the phase he termed 'high-$(Na,Li)_2SiO_3$ solid solution'. It was produced by rapid quenching (in ~1 s) of approximately equimolar compositions, $Na_{2-x}Li_xSiO_3$ with $0{\cdot}86 \le x \le 1{\cdot}02$, from above ~1083 K; *i.e.* from just below the solidus to room temperature. Slower (air) cooling (in ~20 s) produced a phase of closely-related structure termed 'low-$(Na,Li)_2SiO_3$'. (Still slower cooling yielded phase mixtures of Na-rich and Li-rich solid solutions.)

High-$(Na,Li)_2SiO_3$ has a subcell identical to the unit cells of both Na_2SiO_3 and Li_2SiO_3: orthorhombic, space group $Cmc2_1$† (*cf.* Fig. 1). But its diffraction patterns contain additional, satellite reflections indicating a modulation along **b**. The Bravais lattice of low-$(Na,Li)_2SiO_3$ is a slight monoclinic distortion of this orthorhombic subcell: diffraction patterns contain no satellite reflections; but the product was invariably twinned on (100).

West (1977) reported that the magnitude of the primary modulation wavevector, **q**, characteristic of the high-$(Na,Li)_2SiO_3$ structure, varied linearly with composition (x in $Na_{2-x}Li_xSiO_3$), and was a rational number (corresponding to the existence of a superstructure) for simple Na/Li ratios; *e.g.* $\mathbf{q} = \mathbf{b}^*/6$ for Na/Li = 1 ($x = 1{\cdot}00$) and (slightly extrapolated) $\mathbf{b}^*/5$ for Na/Li = 5/4 ($x = 0{\cdot}89$). He commented that simple Na,Li ordering would not be expected to give such long-period superstructures. Nevertheless, the satellite reflections were attributed to long-range ordering of Na and Li (together with atomic displacements along **b***), an interpretation supported by the composition dependence of the magnitude of the modulation wavevector, $|\mathbf{q}|$, and occurrence of rational values of $|\mathbf{q}|$ for simple ratios Na/Li.

He also reported that the (single-crystal) diffraction patterns from some specimens showed considerable streaking in the **b*** direction, and suggested that it could be caused by very fine-scale incipient inversion pheno-

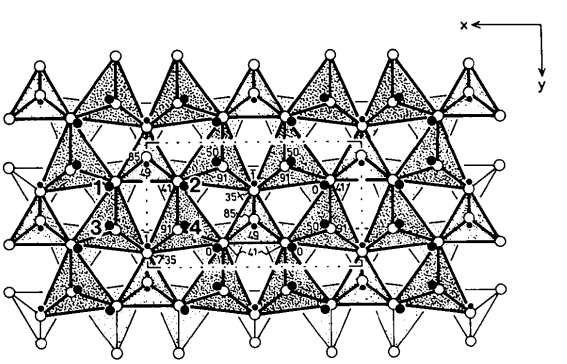

Fig. 1. Structure of Li_2SiO_3. The large tetrahedra are LiO_4 while the smaller tetrahedra are SiO_4. The unit cell is outlined and the four potential Na/Li sites per primitive unit cell are labelled 1 to 4.

† The standard setting; West (1976, 1977) used the nonstandard $Ccm2_1$.

0108-7681/89/020136-06$03.00